2018

Fe73.5Si13.5B9Cu1Nb3 metallic glass: Rapid activation of peroxymonosulfate towards ultrafast Eosin Y degradation

Jincheng Wang
Edith Cowan University

Zhe Jia
Edith Cowan University

Peng Qin
Edith Cowan University

W. C. Zhang

M. D. Wang

See next page for additional authors

10.1016/j.matdes.2017.11.049
Wang, J. C., Jia, Z., Liang, S. X., Qin, P., Zhang, W. C., Wang, W. M., ... & Zhang, L. C. (2018). Fe73. 5Si13. 5B9Cu1Nb3 metallic glass: Rapid activation of peroxymonosulfate towards ultrafast Eosin Y degradation. *Materials & Design*, *140*, 73-84. doi:10.1016/j.matdes.2017.11.049 Available here.

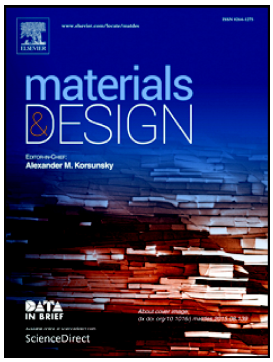

Fe73.5Si13.5B9Cu1Nb3 metallic glass: Rapid activation of peroxymonosulfate towards ultrafast Eosin Y degradation

J.C. Wang, Z. Jia, S.X. Liang, P. Qin, W.C. Zhang, W.M. Wang, T.B. Sercombe, L.C. Zhang

PII: S0264-1275(17)31079-1
DOI: doi:10.1016/j.matdes.2017.11.049
Reference: JMADE 3526

To appear in: *Materials & Design*

Received date: 6 September 2017
Revised date: 20 November 2017
Accepted date: 21 November 2017

Please cite this article as: J.C. Wang, Z. Jia, S.X. Liang, P. Qin, W.C. Zhang, W.M. Wang, T.B. Sercombe, L.C. Zhang , Fe73.5Si13.5B9Cu1Nb3 metallic glass: Rapid activation of peroxymonosulfate towards ultrafast Eosin Y degradation. The address for the corresponding author was captured as affiliation for all authors. Please check if appropriate. Jmade(2017), doi:10.1016/j.matdes.2017.11.049

$Fe_{73.5}Si_{13.5}B_9Cu_1Nb_3$ metallic glass: Rapid activation of peroxymonosulfate towards ultrafast Eosin Y degradation

*J.C. Wang[a], Z. Jia[a,b], S.X. Liang[a], P. Qin[a], W.C. Zhang[c], W.M. Wang[d,**], T.B. Sercombe[e], L.C. Zhang[a,*]*

[a]*School of Engineering, Edith Cowan University, 270 Joondalup Drive, Joondalup, Perth, WA 6027, Australia*

[b]*Department of Mechanical and Biomedical Engineering, City University of Hong Kong, 83 Tat Chee Avenue, Kowloon, China*

[c]*Environmental Protection Administration of Ji'an City, Ji'an, Jiangxi Province, 343000, China*

[d]*School of Materials Science and Engineering, Shandong University, Jinan, Shandong 250061, China*

[e]*School of Mechanical and Chemical Engineering, M050, The University of Western Australia, 35 Stirling Highway, Crawley, Perth, WA 6009, Australia*

[*]Corresponding author. Tel: +61 8 6304 2322; fax: +61 8 6304 5811; email addresses: l.zhang@ecu.edu.au; lczhangimr@gmail.com

[**]Co-corresponding author. +86 531 88392749; email address: weiminw@sdu.edu.cn

Abstract

Discovering functional applications of metallic glasses (MGs) as heterogeneous catalysts is a fundamental and essential topic. This work reports the rapid production of sulfate radicals ($SO_4^{\bullet-}$) from peroxymonosulfate (PMS) using $Fe_{73.5}Si_{13.5}B_9Cu_1Nb_3$ glassy ribbons as catalysts for Eosin Y (EY) dye wastewater treatment. The reaction rates (*k*) from the experimental data reveal that the EY degradation is well fitted with the pseudo-first-order kinetic model. The strong electron transfer ability is characterized by electrochemical methods, presenting an advanced catalytic performance for EY degradation. Various experimental parameters, including dye concentration, catalyst dosage, PMS concentration, light intensity, pH and reaction temperature as well as the saline and natural inorganic effects, are fully investigated. The results show that the color removal of EY dye could achieve nearly 100% within 20 min. The quenching experiments are performed to verify the production of reactive species, suggesting that both •OH and $SO_4^{\bullet-}$ are produced from PMS that play significant roles for EY degradation. This critical study reveals that using $Fe_{73.5}Si_{13.5}B_9Cu_1Nb_3$ MGs as catalysts exhibit a superior reactivity on PMS activation in wastewater treatment. The discoveries shed lights into the study of electron transfer ability for MGs, presenting extensive prospects in the application of dye wastewater treatment.

Keywords: Metallic glass; Heterogeneous catalysis; Peroxymonosulfate; Sulfate radicals; Eosin Y

1. Introduction

Metallic glasses (MGs) have been extensively employed as either structural [1] or functional materials [2] in industries due to their superior physical and chemical properties such as high strength [3, 4], excellent corrosion resistance [5, 6], and soft magnetic properties [7, 8]. However, the development of bulk metallic glasses (BMGs) still has many obstacles, such as the absence of plasticity [9]. Recent reports demonstrate that thin film MGs with enhanced mechanical properties present great potential application in the catalytic research field [10, 11]. To date, MGs with various elemental compositions have been widely studied as effective catalysts for industrial effluents treatment [12-15]. It has been reported that the $Fe_{78}Si_9B_{13}$ and $Fe_{73.5}Si_{13.5}B_9Cu_1Nb_3$ MGs demonstrate 5 - 10 times quicker production rate of reactive species than the currently employed Fe-based catalysts [16]. The $Fe_{76}B_{12}Si_9Y_3$ MG powders show 1000 times higher reactivity than crystalline Fe powders in treating methyl orange [17]. In addition to their superior reusability, the $Fe_{76}B_{12}Si_9Y_3$ MG powders and ribbons could be reused up to 13 cycles in methyl orange degradation [17] and more than 30 times in degrading methyl blue without significantly loosing efficiency [18], respectively. These catalytic performances show that using amorphous alloys as catalysts would provide better efficiency than the traditional crystalline catalysts. However, the catalytic mechanism is still not yet clear.

Conventional techniques, such as physical, biological, and chemical approaches, have been widely explored to remove various dye effluents. The physical treatments achieve removal of toxic organics by naturally occurring forces without altering the nature of organics. Biological methods are ineffective because the microorganisms are less resistant to the complex aromatic structure of dye effluents [19]. The traditional chemical method always causes seriously secondary pollution. Recently, advanced oxidation processes (AOPs), which combining chemical and advanced material technologies are rapidly developed, such as

ozone (O_3) oxidation [20], Fenton/Fenton-like process [21-23], and photocatalysis [24-26]. The superiority of the AOPs is that the reactive species, such as hydroxyl radicals (•OH) and sulfate radicals ($SO_4^{\bullet-}$), can be generated to effectively oxidize organic matters from effluents into H_2O, CO_2, and other harmlessly inorganic molecules [24]. Very recently, largely due to the superior features of abundant natural source, low cost, and friendly environmental compatibility, Fe-based heterogeneous catalysts have been extensively investigated for their performance in AOPs, such as goethite (α-FeOOH) [27], magnetite (Fe_3O_4) [28], hematite (α-Fe_2O_3) [29], maghemite (g-Fe_2O_3) [30], and zero-valent iron (ZVI) [31]. However, these catalysts still have significant disadvantages, such as low efficiency, less reusable, fast decay, and secondary pollution [21]. Recent reports demonstrate that using MGs as catalysts could effectively overcome the abovementioned shortcomings and their catalytic activity could be much improved by tuning their particle size [32], surface morphology [33], surface to volume ratio [5], and chemical composition [14, 15]. For example, the $Fe_{73.5}Si_{13.5}B_9Cu_1Nb_3$ MGs can be used as an effective catalyst in activation of hydrogen peroxide (H_2O_2) to rapidly generate hydroxyl radicals (•OH) for completely degrading methyl blue and methyl orange within 20 min [16]. Compared to the •OH with the redox potential of E° = 2.7 - 2.8 V [34] and the short half-life of 10^{-3} μs [35], the $SO_4^{\bullet-}$ with a similar redox potential of E° = 2.5 - 3.1 V [36] has a much longer stability (half-life 30 - 40 μs) in the dye effluents [35, 37]. In addition to the reactive environment, the Fe^{2+}/H_2O_2 system is preferred at pH range from 2 - 6, which largely limits the actual industrialization. In comparison, the broad operative pH range of the $SO_4^{\bullet-}$ [37] is the second attractive property in water treatment. According to Nidheesh and Rajan [38], the AOPs involved $SO_4^{\bullet-}$ have a higher removal efficiency for pollutants and can be used in a wide pH range (i.e. 3, 6 and 9). Peroxymonosulfate (PMS) [39, 40] and persulfate (PS) [41] are two important resources for producing the $SO_4^{\bullet-}$. Traditionally, the $SO_4^{\bullet-}$ can be generated by the homogeneous energetic

activation of UV [42] or thermal activation [43] and heterogeneous catalytic activation of metal-free catalysts [44] or metal-based catalysts [45]. Especially, the reaction rate of $SO_4^{\bullet-}$ by homogeneously energetic activation (e.g. heat, $k = 1.0 \times 10^{-7}$ $M^{-1} \cdot s^{-1}$ [46]) is much lower than heterogeneously catalytic activation by transition metals, such as using iron as the catalyst with the reaction rate of $k = 2.0 \times 10^{1}$ $M^{-1} \cdot s^{-1}$ [46]. However, the most important drawback to the transition metals/$SO_4^{\bullet-}$ system is that the leached metallic ions would react with the PS/PMS to reduce the activation rate, and the salinity as well as natural inorganic ions in the water would consume the generated $SO_4^{\bullet-}$. According to those aforementioned advantages and disadvantages, developing an advanced catalyst that has high efficiency in catalytic activation of $SO_4^{\bullet-}$ and low leaching rate of the transition metals as well as the effect of the salinity or natural inorganic ions for degrading contaminants in wastewater is always a challenging topic.

Eosin Y (EY), also named as Acid Red 87, is a xanthene red dye that defined as a conjugated π system [47]. The EY dye is broadly used in dyeing, printing, leather, and fluorescent pigment, and painting industries because of its low prices and bright color. The carcinogenicity of EY has been experimentally confirmed, and the acute poisonousness of the dye can lead to a variety of chronic effects to the health of inhabitants and damages to the environment [48]. Therefore, to explore an effective, low cost, and environmental-friendly catalyst is increasingly concerned in the textile or paper industry. This work reports the sulfate radicals ($SO_4^{\bullet-}$) and hydroxyl radicals (•OH) activation from PMS using $Fe_{73.5}Si_{13.5}B_9Cu_1Nb_3$ MGs under heterogeneous Fenton-like process. Initially, the amorphous nature of the manufactured $Fe_{73.5}Si_{13.5}B_9Cu_1Nb_3$ MGs glassy ribbon is characterized by XRD and the surface morphology is analyzed by SEM. The electrochemical performance in simulated solution is also performed to examine electron transfer and corrosion resistance abilities of the glassy ribbons. The influenced factors on EY dye degradation efficiencies are

systematically examined, and the corresponding pseudo-first-order reaction kinetic rates (*k*) are thoroughly studied.

2. Materials and methods

2.1. Materials

The metallic glass with a nominal atomic composition of $Fe_{73.5}Si_{13.5}B_9Cu_1Nb_3$ was prepared by arc melting of a mixture of Fe, Si, B, Cu and Nb with purity higher than 99.9 wt.% under a Ti-gettered argon atmosphere. The melted master ingot was melted by induction heating in a quartz crucible, and then the molten master ingot was ejected onto a chilled copper roll surface with a rotating speed of 5 - 39 m/s and then fast quenched. Afterwards, the as-quenched ribbons have an approximate thickness of 30 - 40 μm and a width of 5mm [49]. The Eosin Y used throughout this experiment was obtained from Ji'an Haomai Fine Chemical Industry Co., Ltd. (China). The characteristics of EY are summarized in Table 1. The peroxymonosulfate and *tert*-butanol (TBA, ≥ 99%) were purchased from Sigma-Aldrich. Ethanol (absolute, EtOH) was purchased from Merck. All other chemicals and reagents, such as NaOH, H_2SO_4, HCl, HNO_3, humic acid (HA), NaCl, $NaNO_2$ were at analytical grades, and used without further purification. All the required sample solutions were diluted with Milli-Q water (18.2 MΩ·cm) throughout the experiments.

Table 1

Characteristics and structure of Eosin Y dye.

Empirical formula	$C_{20}H_6Br_4Na_2O_5$
Molecular weight (g/mol)	691.85
λ_{max} (nm)	516
Structure	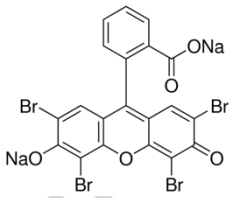

2.2. Characterizations

The structural characteristic and phase contents of the fabricated glassy ribbons were characterized by X-ray diffraction (XRD, PANalytical Empyrean, Netherlands) with Co-Kα radiation (λ = 0.179 nm). The surface morphologies of glassy ribbons before and after reactions were characterized by using a Scanning Electron Microscope (SEM) outfitted with EDS (JEOL 6000, Japan). Electrochemical tests of the $Fe_{73.5}Si_{13.5}B_9Cu_1Nb_3$ glassy ribbons were conducted in a beaker containing sulfuric acid (H_2SO_4) solution at pH is equal to 3.4 (same as the experimental condition after adding PMS into dye solution). All electrochemical measurements were recorded by electrochemical workstation (PARSTAT 2273) in a conventional three-electrode cell, where the $Fe_{73.5}Si_{13.5}B_9Cu_1Nb_3$ ribbon was used as working electrode with an exposed surface area of approximately 1.0 cm^2. A platinum net applied as the counter electrode, and a saturated calomel electrode (SCE) served as the reference electrode, which connected to a Luggin capillary bridge. All the potential recorded and mentioned in this electrochemical measurement section were versus SCE. The potentiodynamic polarization measurement was performed at a scan rate of 0.1667 mV/s. The cathodic polarization curve starting from -0.5 V and scanned to the potential of +2 V at anodic polarization region. The electrochemical impedance spectroscopy (EIS) was probed at

open circuit potential (OCP) potentiostatically, and performed with an AC amplitude of 5 mV over the frequency range from 10^{-2} to 10^{4} Hz. The OCP of $Fe_{73.5}Si_{13.5}B_9Cu_1Nb_3$ ribbon was acquired by raising immersion time from 0 to 16 hours. The ZSimpWin software was used to fit the electrochemical impedance data, which were interpreted by a specific electrical equivalent circuit. For the measurements of total organic carbon (TOC), an excessive $NaNO_2$ solution (0.1 M) was used to quench the reaction, following by a TOC analyzer (TOC-V_{CSH}, Shimadzu, Japan) for the mineralization analysis. For Fe and Nb leaching experiments, 2% v/v nitric acid (HNO_3) was used to dilute the samples and then filtered by the 0.22 μm filter before the trace element analysis (iCAP Q ICP-MS, Thermo Fisher Scientific, USA). The pH of dye solution was measured by a pH meter (Oakton PC 2700 Benchtop Meter, Oakton Instruments, USA).

2.3. Methods

Eosin Y dye was used to study the catalytic activity of the $Fe_{73.5}Si_{13.5}B_9Cu_1Nb_3$ glassy ribbons. All tests were implemented in a 250 ml beaker containing with 100 ml specific concentration of dye solution. A Vortex-Genie 2 mixer (Scientific Industries, USA) and a solar light (Perfectlight, China) were utilized for stirring and irradiating dye solutions, respectively. The catalytic activity was measured at the predetermined time intervals using Perkin Elmer Lambda 35 UV–vis spectrometer (Shelton, CT, USA), which can determine the variation of dye concentration as a function of absorbance peak value. For constant temperature experiments, the beaker was put into a thermostatic water bath with the predetermined temperature at 25 °C, 30 °C, 40 °C, 50 °C, and 60 °C. The initial pH of dye was measured as 5.8. The H_2SO_4 solution was prepared by using analytical grades of NaOH (0.1 M) and H_2SO_4 (0.1 M) with Milli-Q water to simulate the favorable pH of dye degradation. The experimental parameters were briefed in Table 2.

Table 2

Summarized experimental parameters.

Parameter	Value
$Fe_{73.5}Si_{13.5}B_9Cu_1Nb_3$ dosage (g/L)	0-2.0
Initial dye concentration (ppm)	20-120
Irradiation intensity ($\mu W/cm^2$)	0-14.8
PMS concentration (mM)	0-2.0
pH	3.4-11.5
Temperature ($^{\circ}C$)	25-60
Reaction time (min)	up to 50

The characteristic absorption peak of Eosin Y was measured to be λ_{max} = 516 nm. Eq. (1) computed the color removal rate of EY solution:

$$X(\%) = 100\% \times (C_0 - C)/ C_0 \quad (1)$$

where C_0 is the initial concentration at t = 0 and C is the concentration of EY dye at time t. The equation of the pseudo-first-order kinetic reaction model was estimated using Eq. (2):

$$ln (C_0/ C) = k_{obs} t \quad (2)$$

where k_{obs} (min^{-1}) is the kinetic rate constant, C_0 is the initial concentration at t = 0 and C is the concentration of EY dye at time t.

3. Results and discussion

3.1. Catalyst characterization

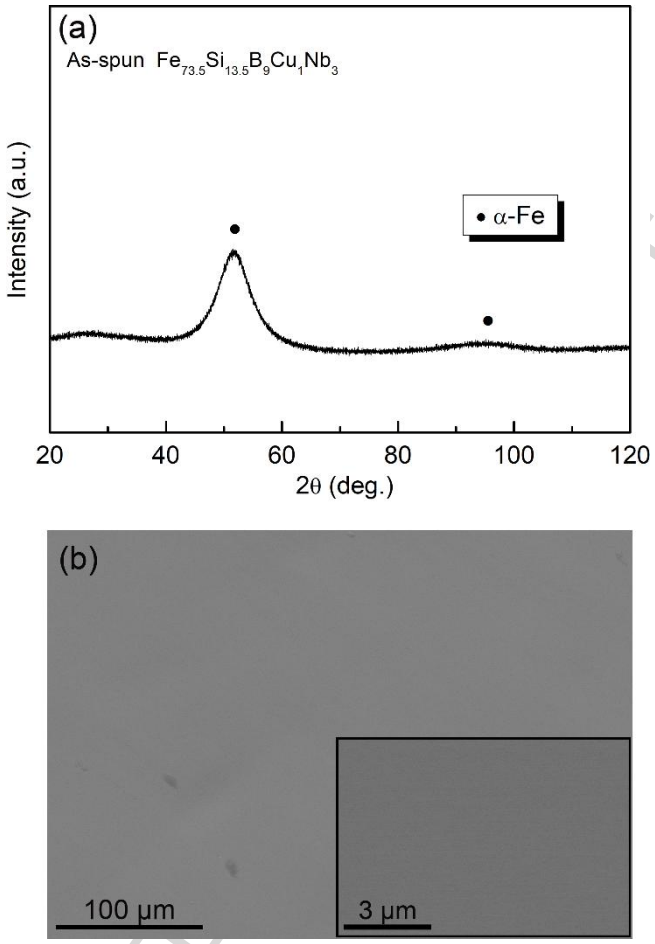

Fig. 1. (a) XRD pattern and (b) SEM micrograph (inset shows a corresponding zoom-in SEM micrograph) for the as-spun $Fe_{73.5}Si_{13.5}B_9Cu_1Nb_3$ glassy ribbons.

Fig. 1(a) shows the XRD pattern of the as-spun $Fe_{73.5}Si_{13.5}B_9Cu_1Nb_3$ glassy ribbons. It can be clearly seen that a board diffuse diffraction peak presented in the 2θ domain of 40° - 60°, representing that the amorphous phase of the glassy ribbon is predominant [50, 51]. Fig. 1(b) displays the SEM image of the $Fe_{73.5}Si_{13.5}B_9Cu_1Nb_3$ glassy ribbons, indicating that the initial surface of the sample is smooth and defectless. Further demonstration can be seen from the inset of corresponding SEM image, which is also hard to find any apparent defect on the materials surface.

3.2. Electrocatalytic performance

MGs have been attracting extensive attention in wastewater treatment due to their excellent corrosion resistance behavior [52-54]. As shown in Fig. 2, the potentiodynamic polarization curve and EIS measurements are recorded after observing a relatively stable OCP of the $Fe_{73.5}Si_{13.5}B_9Cu_1Nb_3$ glassy ribbon. Fig. 2(a) shows the potentiodynamic polarization curve that is characterized from cathodic and anodic polarization region. Notably, no standard Tafel region can be observed, but it can be clearly seen that the corrosion potential of the glassy ribbon is approximately at -0.35 V, which is much higher than the MgZn-based MGs (-1V) [12] and slightly greater than the $Fe_{78}Si_9B_{13}$ glassy ribbon (-0.6V) [55]. This result proves that the $Fe_{73.5}Si_{13.5}B_9Cu_1Nb_3$ glassy ribbon has a strong corrosion resistance campared to the other two MGs. With respect to the anodic region of the polarization curve, unlike the 316L stainless steel [56] or other coated materials with superior corrosion resistance, the manufactured $Fe_{73.5}Si_{13.5}B_9Cu_1Nb_3$ glassy ribbon does not present passivation behavior. Furthermore, the anodic polarization curve shows a continuous dissolution and the curve extends to the potential of 2V even without any pitting behavior. This phenomenon indicates an excellent corrosion resistance of $Fe_{73.5}Si_{13.5}B_9Cu_1Nb_3$ MGs in withstanding the localized corrosion under the acid solution [52]. Fig. 2(a) inset presents the stabilization progress of open circuit potential (OCP) against the immersion time. The reduction of the OCP in the first two hours reveals a dissolution stage of the active metal immersed in acidic solution, and the main dissolution element is Fe. The lowest OCP has been observed at the immersion time of 2 hours, and the cationic metal ion at this stage has reached its critical point in the test solution. After passing this point, the OCP has a quickly positive move in the next 1 hour. This stage involves the swift development of passivation by fast electron transfer on the ribbon surface, which would lead to high chemical reactivity in dye degradation. After the immersion time of 3 hours, the OCP curve moves along a flat line

and trends to stable while the time approaches to 16 hours. During this period, the electrons between the ribbon surface and the test solution have a relatively stable state, providing a protective film on the ribbon surface. The produced film would definitely improve the sustainability and reusability of the manufactured $Fe_{73.5}Si_{13.5}B_9Cu_1Nb_3$ catalysts in the wastewater treatment. The stable and protective passive film on the metal surface is mainly formed by chemical reactions of the Fe, Si, and Nb [57] atoms, where the atoms are progressively hydrated or oxidized to γ-FeO(OH) [58], SiO_2 [33], and Nb_2O_5 [16], respectively. As shown in Figs. 2(b) and (c), the electrochemical impedance spectroscopy (EIS) measurements demonstrate the analysis in the shape of Nyquist and Bode plots for the $Fe_{73.5}Si_{13.5}B_9Cu_1Nb_3$ glassy ribbons. The EIS Nyquist plot is relevant to the electron transfer resistance. The radius of the semi-circular arc in the Nyquist curve indicates the interface layer resistance existing on the electrode surface and a smaller semi-cicular arc radius means a lower electron transfer resistance [59]. From the Nyquist plot (Fig. 2b), two capacitive arcs with small radius are observed. Comparing with semi-cicular arc radiuses of different partially crystallized $Fe_{78}Si_9B_{13}$ MGs [55], the relatively small radius of $Fe_{73.5}Si_{13.5}B_9Cu_1Nb_3$ MGs reveals a low polarization resistance of the passive film, presenting a considerably strong electron transfer ability on the metal surface [55]. Considering the Nyquist plot (Fig. 2b) and the Bode plot (Fig. 2c), two times constant equivalent circuit module (Fig. 2d) is used to fit the EIS results. The circuit model constitutes with a parallel combination of a constant phase element (CPE_2) and a charge transfer resistance (R_{ct}), in cascade with the passive film resistance (R_f), and then parallel with another constant phase element (CPE_1) and next in series connected with solution resistance (R_s). The using of CPE_1 and CPE_2 are because the material surface is never ideal flat, it is normally considered as a rough or defective layer on the surface of the electrode [60]. As can be seen from Figs. 2(b) and (c), the obtained results from potentiodynamic measurements and EIS data are in very good agreement.

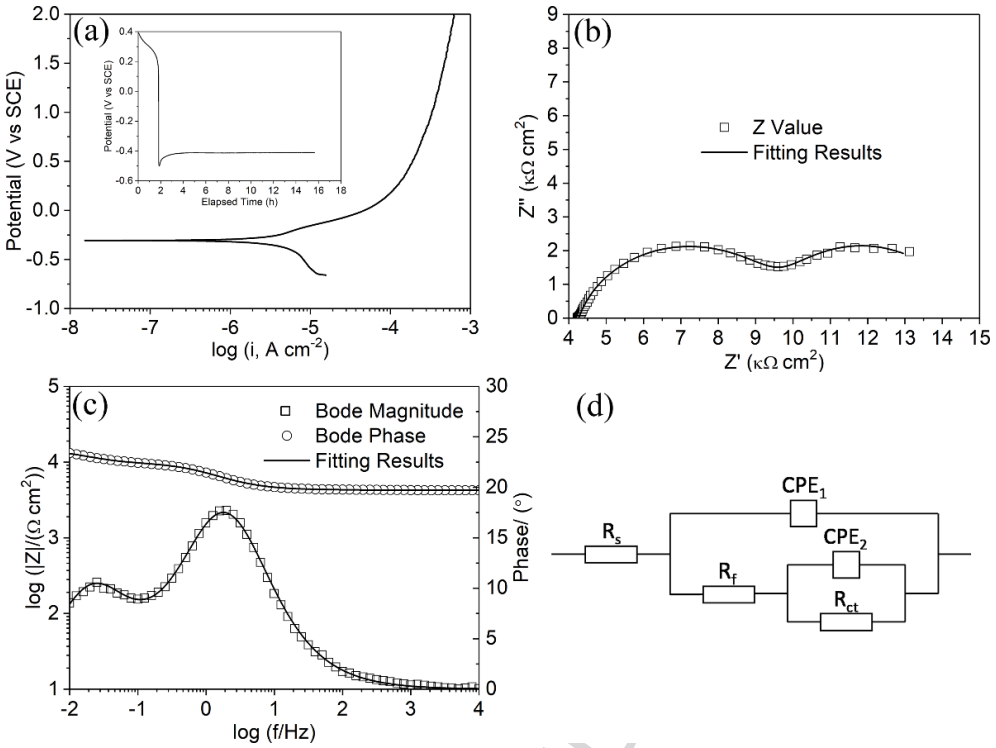

Fig. 2. (a) The potentiodynamic polarization curve (inset shows open circuit potential (OCP) as function of time), the EIS results in the form of (b) nyquist plots, (c) bode plots and (d) electrical equivalent circuit used for impedance spectra analysis for $Fe_{73.5}Si_{13.5}B_9Cu_1Nb_3$ glassy ribbons in aerated H_2SO_4 solution of pH 3.4 at room temperature.

3.3. Catalytic evaluation

3.3.1. Dye degradation and efficiency

To confirm the effects of various experimental parameters on EY degradation efficiency, the comparable results of color removals using as-spun $Fe_{73.5}Si_{13.5}B_9Cu_1Nb_3$ MGs and the corresponding reaction rates (k) are shown in Fig. 3 and Table 3, respectively. Fig. 3(a) shows the effect of EY concentration in the range of 20 - 120 ppm. It can be seen that the color removal rate slightly decreases when EY initial concentration increases. At 20 ppm of EY dye solution, the color removal rate reaches 95% within 10 min and the reaction rate (k) can be achieved at k = 0.876 min^{-1}. By comparison, the color removal rate only rises to 72% with k = 0.170 min^{-1} for the initial concentration of 120 ppm within the same time. The possible reasons are that: 1) increasing the concentration of EY dye, more organic dye

molecules would adsorb on the ribbon surface and thus blocking the reaction of Fe and PMS; 2) the produced reactive species from ribbon surface are not sufficient to consume extra organic molecules within the same time intervals; 3) the increased number of molecules could increase the optical density of solution, leading to less UV-vis light energy being transferred for producing $SO_4^{\bullet -}$ from PMS [25, 41].

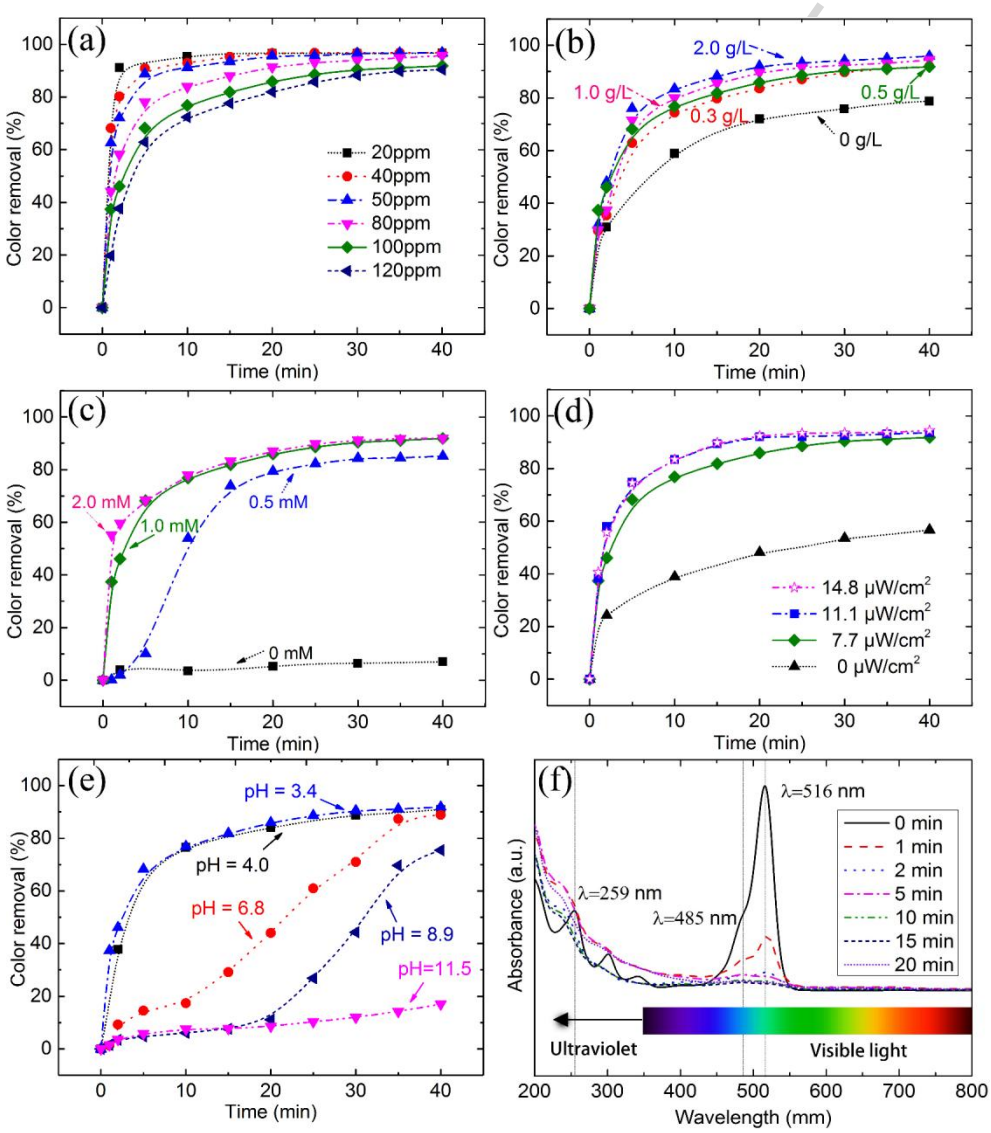

Fig. 3. Comparison of color removals for Eosin Y dye by using: as-spun $Fe_{73.5}Si_{13.5}B_9Cu_1Nb_3$ MGs as function of (a) dye concentration, (b) catalyst dosage, (c) PMS concentration, (d) irradiation intensity and (e) pH; (f) UV-vis spectra changes of Eosin Y dye in the presence of the $Fe_{73.5}Si_{13.5}B_9Cu_1Nb_3$ metallic glass/UV-vis/PMS at different time intervals (if not mentioned, the conditions are catalyst dosage: 0.5 g/L, irradiation intensity: 7.7 μW/cm^2, dye concentration: 100 ppm, and PMS concentration: 1.0 mM)

Table 3

Kinetic reaction rates (k) over various experimental parameters

Dye concentration (ppm)	PMS concentration (mM)	Dosage (g/L)	Irradiation intensity ($\mu W/cm^2$)	pH	Temperature ($^{\circ}C$)	k (min^{-1})
20	1.0	0.5	7.7	3.4	25	0.876
40	1.0	0.5	7.7	3.4	25	0.477
50	1.0	0.5	7.7	3.4	25	0.303
80	1.0	0.5	7.7	3.4	25	0.230
100	1.0	0.5	7.7	3.4	25	0.171
120	1.0	0.5	7.7	3.4	25	0.170
100	1.0	0	7.7	3.4	25	0.073
100	1.0	0.3	7.7	3.4	25	0.166
100	1.0	0.5	7.7	3.4	25	0.171
100	1.0	1.0	7.7	3.4	25	0.235
100	1.0	2.0	7.7	3.4	25	0.260
100	0.0	0.5	7.7	3.4	25	0.001
100	0.5	0.5	7.7	3.4	25	0.098
100	1.0	0.5	7.7	3.4	25	0.171
100	2.0	0.5	7.7	3.4	25	0.189
100	1.0	0.5	0.0	3.4	25	0.033
100	1.0	0.5	7.7	3.4	25	0.171
100	1.0	0.5	11.1	3.4	25	0.212
100	1.0	0.5	14.8	3.4	25	0.205

100	1.0	0.5	7.7	3.4	25	0.171
100	1.0	0.5	7.7	4.0	25	0.180
100	1.0	0.5	7.7	6.8	25	0.072
100	1.0	0.5	7.7	8.9	25	0.069
100	1.0	0.5	7.7	11.5	25	0.010
100	1.0	0.5	0	3.4	25	0.021
100	1.0	0.5	0	3.4	30	0.023
100	1.0	0.5	0	3.4	40	0.032
100	1.0	0.5	0	3.4	50	0.045
100	1.0	0.5	0	3.4	60	0.051

Fig. 3(b) shows the effect of catalyst dosage on dye degradation. It can be seen that only 58% of EY dye degradation with k = 0.073 min^{-1} is reached within 10 min by only using PMS under UV-vis irradiation and 78% of color removal achieved at 40 min. When the dosage of $Fe_{73.5}Si_{13.5}B_9Cu_1Nb_3$ MGs increases from 0 g/L to 0.5 g/L, the EY dye degradation rate significantly rises from 58% to 76% within 10 min and the reaction rate k increases from k = 0.073 min^{-1} to k = 0.171 min^{-1}, respectively, owing to a large amount of $SO_4^{\bullet -}$ from PMS (Eqs. 3 and 4) are activated from the $Fe_{73.5}Si_{13.5}B_9Cu_1Nb_3$ glassy ribbon. Further increasing the dosage from 0.5 g/L to 2.0 g/L could only slightly enhance the decolorization rate. The results indicate that excessive ribbon dosages would not act as the scavenger of $SO_4^{\bullet -}$ (Eq. 5) because $Fe_{73.5}Si_{13.5}B_9Cu_1Nb_3$ metallic glass has superior surface stability, resulting in the relatively lower leaching of Fe ions (Fe^{2+} or Fe^{3+}) [16, 41]. The reason behinds the better performance is that both of the Fe^0 and Fe^{2+} (Eqs. 3 and 4) can react with PMS to generate $SO_4^{\bullet -}$. Considering the effective utilization of the catalyst, 0.5 g/L is treated as the referenced dosage for the following experiments. Variation of PMS concentration is another significant

parameter in the dye degradation. Fig. 3(c) shows the influences of PMS concentration on EY dye degradation. Only less than 8% of EY decolorization with k = 0.001 min^{-1} could be reached by solely adding $Fe_{73.5}Si_{13.5}B_9Cu_1Nb_3$ MGs within 50 min, which is possibly caused by dye molecules adsorbtion on the surface of $Fe_{73.5}Si_{13.5}B_9Cu_1Nb_3$ MGs. When increasing the PMS concentration to 0.5 mM, the dye degradation efficiency sharply increases to 73% within 15 min with k = 0.098 min^{-1}. Such performance suggests that a certain quantity of $SO_4•^-$ (Eqs. 3 and 4) are swiftly activated by the $Fe_{73.5}Si_{13.5}B_9Cu_1Nb_3$ MGs from a very low PMS concentration. At higher concentration, such as 1.0 mM, the excessive HSO_5^- from PMS may react with the Fe^{3+} to re-produce Fe^{2+} (Eq. 6), which could further enhance the production of $SO_4•^-$. However, further increasing PMS concentration from 1.0 mM to 2.0 mM only shows a very slight rise of decolorization rate from 81% to 83% within 15 min. It is attributed to the scavenging effect of excessive HSO_5^- and the generation of less reactive $SO_5•^-$ (E° = 1.1 V) (Eq. 7) in the reactive system [61]. Fig. 3(d) shows the effect of irradiation intensity from 0 to 14.8 μW/cm^2 on EY dye color removal. Interestingly, the EY dye degradation without light irradiation can only achieve 56% at 40 min with k = 0.033 min^{-1}, indicating that sole $Fe_{73.5}Si_{13.5}B_9Cu_1Nb_3$ MGs could activate PMS. While increasing the light intensity to 7.7 μW/cm^2, the color removal sharply improving to 85% at 20 min with k = 0.171 min^{-1}. Further increasing irradiation intensity from 7.7 to 11.1 μW/cm^2 could improve the color removal from 85% to 92% within 20 min. The effect of the dye degradation is negligible when further increasing the intensity to 14.8 μW/cm^2. The proposed reason is that the photochemical conversion from Fe^0 to Fe^{2+} and Fe^{3+} to Fe^{2+} could be enhanced by the light energy, providing more active Fe^{2+} source to react with PMS. Also the simulated UV-vis irradiation could assist the activation of PMS to produce extra •OH and $SO_4•^-$ (Eqs. 8 and 9). Consequently, the generated •OH and $SO_4•^-$ could oxidize organic molecules into non-toxic by-products (Eq. 10). In addition, the effect of pH plays a significant role in the Fenton-

like process. Fig. 3(e) indicates the effect of solution pH after adding PMS on the EY degradation. Initially, the dye solution pHs are 5.8, 9.0, 10.0, 11.0 and 12.0. After adding 1.0 mM PMS, the corresponding pHs are 3.4, 4.0, 6.8, 8.9 and 11.5, respectively, which have been shown in Fig. 3(e). It should be known that the fastest decolorization occurs at the pH of 3.4, which is favorable for the Fenton-like reaction [16]. The acidic nature of PMS leads to the similar reaction rate k = 0.171 min^{-1} and 0.180 min^{-1} for pH of 3.4 and 4.0, respectively. On the other hand, both pHs of 6.8 and 8.9 experience a two-stage reaction: a very slow decolorization process and a sudden increase. The possible explanation is that under the neutral and weak alkaline conditions, PMS is mainly activated by irradiation to produce •OH and SO_4•$^-$ (Eq. 9) with a slow rate. Part of SO_4•$^-$ subsequently react with PMS to generate H^+ (Eq. 7). Then the pH become lower (results not shown) until the condition is satisfied for ribbons to rapidly activate PMS. In the alkaline condition of 11.5, the ribbons surface is highly passivated and degradation efficiency also decreases.

$$Fe^0 + 2HSO_5^- \rightarrow Fe^{2+} + 2OH^- + 2SO_4 \bullet^- \quad (3)$$

$$Fe^{2+} + HSO_5^- \rightarrow Fe^{3+} + OH^- + SO_4 \bullet^- \quad (4)$$

$$Fe^{2+} + SO_4 \bullet^- \rightarrow Fe^{3+} + {SO_4}^{2-} \quad (5)$$

$$Fe^{3+} + HSO_5^- \rightarrow Fe^{2+} + H^+ + SO_5 \bullet^- \quad (6)$$

$$HSO_5^- + SO_4 \bullet^- \rightarrow {SO_4}^{2-} + H^+ + SO_5 \bullet^- \quad (7)$$

$$Fe(OH)^{2+} + hv \rightarrow \bullet OH + Fe^{2+} \quad (8)$$

$$HSO_5^- + hv \rightarrow \bullet OH + SO_4 \bullet^- \quad (9)$$

$$\bullet OH + SO_4 \bullet^- + organic \rightarrow byproducts + CO_2 + H_2O + {SO_4}^{2-} \quad (10)$$

Fig. 3(f) demonstrates the UV-vis absorbance spectra of Eosin Y dye degradation by using $Fe_{73.5}Si_{13.5}B_9Cu_1Nb_3$ MGs/PMS system. The absorbance intensity decreases as a function of reaction time increases. Three absorption peaks of Eosin Y dye are observed at wavelengths of 259 nm, 485 nm, and 516 nm. The main absorption peak at 516 nm is

ascribed to the initial red color of EY's chromophore. The shoulder peak at 485 nm shows the dimeric substance of EY and the less intense peak at 259 nm corresponds to the $\pi \rightarrow \pi^*$ transitions in the aromatic rings [47]. As can be observed from UV bands during the dye degradation process, the UV absorption bands at $\lambda = 516$ nm and 485 nm in the visible region gradually decrease and become invisible after 20 min, indicating the chromophoric part of the molecules has been destructed. Furthermore, the absorption peak at 259 nm also rapidly decreases with increasing the light irradiation time, denoting that aromatic linkage bonds in EY dye molecules have been gradually mineralized. It suggests that the $Fe_{73.5}Si_{13.5}B_9Cu_1Nb_3$ MGs can effectively activate PMS to generate reactive species, which can efficiently decompose the aromatic rings in dye molecules [62].

In general, the intermediate compounds are very important to be analyzed during the dye degradation process in chemistry. However, the primary objective at the current stage in this work is to investigate the dye degradation efficiency and the mineralization by Fe-based metallic glass. As such, TOC experiments were conducted investigated to prove that the toxic organic dye pollutants have been degraded and mineralized. Fig. 4 verifies the dye degradation and mineralization process. It is observed that TOC removal rate increases with the reaction time and up to 60 % can be reached within 30 min, indicating that the reactive species generated by PMS activation can effectively convert dye molecules into CO_2, H_2O and other harmlessly inorganic substances. Similar TOC removal rate can be achieved with a wide pH range, which is reported by Sarath et al. [63]. However, more than 50% of mineralization rate can be seen within 20 min in this work, indicating a higher efficiency. During the Eosin Y mineralization, the intermediates including 2-(2-formylphenyl)-2-carboxylate, 2-(2-(3,6-dihydro-2H-pyran-4-yl)phenyl)2-carboxylate and 3,5-dibromocyclohex-5-ene-1,2,4-trione are proposed to be generated in the photo-enhanced oxidative degradation [62, 64], after which radical groups on the benzene ring are

substituted and a series of ring opening reactions attacked by •OH and SO_4•$^-$ occur. On the other hand, Fig. 4 shows a low iron (mainly in the form of Fe^{2+} and Fe^{3+}) leaching concentration during PMS activation, demonstrating the advanced surface stability and effective activation efficiency of $Fe_{73.5}Si_{13.5}B_9Cu_1Nb_3$ MGs. Notably, inset of Fig. 4 presents extremely low Nb leaching concentrations which are lower than 10.0 μg/L for all those reaction time, indicating that the Nb on the ribbons surface are very stable and hard to be corroded.

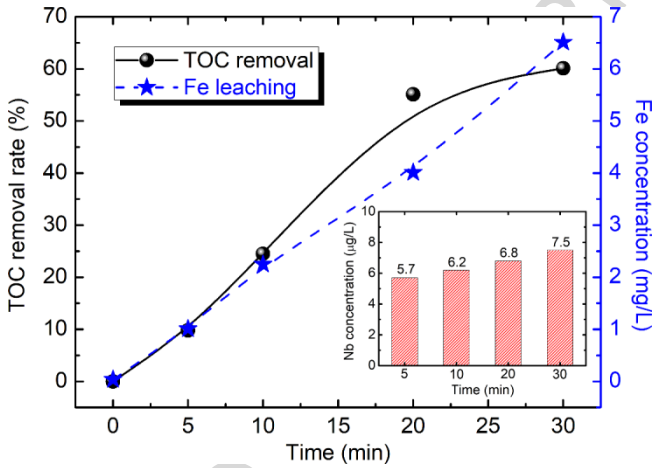

Fig. 4. TOC removal rate of Eosin Y dye (left), Fe leaching concentration (right) and Nb leaching concentration (inset) within 30 min (the conditions are catalyst dosage: 0.5 g/L, irradiation intensity: 7.7 μW/cm^2, dye concentration: 100 ppm, and PMS concentration: 1.0 mM).

3.3.2. Effect of reaction temperatures

Regarding chemical reactions, the reaction temperature is always considered as an important experimental condition. Fig. 5(a) shows the evaluation of the degradation efficiency in the temperature ranging from 25 to 60 °C. Notably, the degradation rate rises along with the increase of temperature. A highest efficiency at the temperature of 60 °C is observed compared to other temperatures. It agrees well with other literatures [65, 66]. Fig. 5(b) illustrates the linear relationship between ln (C_o/C) and reaction time. All the regression coefficients (R^2) are higher than 0.98 for different temperatures, indicating that the kinetic reaction of EY follows well to pseudo first-order kinetic model. The values of k obtained

from the slope of the straight line are 0.023 min^{-1}, 0.032 min^{-1}, 0.045 min^{-1}, and 0.051 min^{-1} at 30 °C, 40 °C, 50 °C, and 60 °C, respectively. The results are summarized in Table 3. Apparently, increasing the reaction temperature will lead to a higher reaction rate.

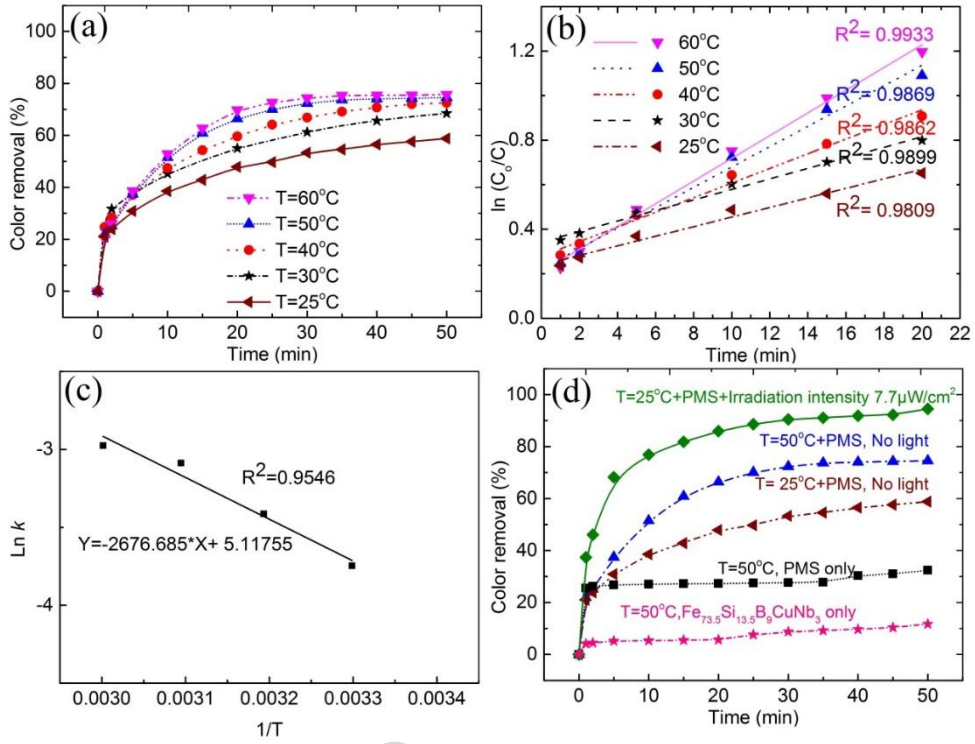

Fig. 5. (a) Effect of temperature on color removal rate in percentage vs. time; (b) variation of ln(C_o/C) vs. time at different temperature intervals (c) Arrhenius plot of ln *k* vs. 1/*T* for the decolorization of EY to determine activation energy; (d) comparison of experimental effect of PMS, irradiation intensity, and temperature for decolorization of EY dye; (if not mentioned, catalyst dosage: 0.5 g/L, irradiation intensity: 0 μW/cm^2, dye concentration: 100 ppm and PMS concentration: 1.0 mM).

Fig. 5(c) depicts the plot of ln *k* verse 1/*T*, where *k* is the acquired kinetic constants at different temperature intervals (in Kelvin). The activation energy (E_a) on the degradation of EY by $Fe_{73.5}Si_{13.5}B_9Cu_1Nb_3$ can be obtained by applying Arrhenius equation (Eq. 11) [67].

$$lnk = -E_a/R_gT + lnA \quad (11)$$

Where *A* is the pre-exponential factor, R_g is the ideal gas constant (8.314 J/K·mol) and *T* is the reaction absolute temperature (K). Based on Eq. (11), the activation energy can be calculated as E_a = 22.2 kJ/mol for EY dye degradation by $Fe_{73.5}Si_{13.5}B_9Cu_1Nb_3$ MGs over the

temperature range from 30 to 60 °C. The result shows that the removal of EY dye is a chemically controlled processes [68]. The activation energy for ordinary thermal reactions using crystalline Fe-based catalysts is between 60 and 250 kJ/mol [69]. Therefore, a lower energy is required for the oxidation reaction process using catalysts with an amorphous structure. As mentioned above in Fig. 5(a), the decolorization is sensitive to the temperature. Thus, it is important to investigate the effects of temperature on this chemical oxidation reaction mechanism. In Fig. 5(d), only 5% and 23% color removal rates are achieved at the temperature of 50 °C after 50 min for the only addition of $Fe_{73.5}Si_{13.5}B_9Cu_1Nb_3$ and PMS, respectively. By adding $Fe_{73.5}Si_{13.5}B_9Cu_1Nb_3$ and PMS without UV-vis irradiation, the raising of temperature from 25 to 50 °C results in the decolorization efficiency increasing from 42% to 66% within 20 min. It reveals that the degradation efficiency can be effectively enhanced at higher reaction temperature. Although both the temperature and UV-vis irradiation are important factors in this oxidation process, it is still not clear that which one has a relative higher contribution during the reactions. From Fig. 5(d), the color removal rate achieves 91% after 50 min at 25°C under the UV-vis irradiation intensity of 7.7 μW/cm^2, while the decolorization efficiency without UV-vis irradiation only reaches 71% after 50 min at 50 °C. It reveals the light irradiation is more favorable than temperature in this degradation process.

3.3.3. Effect of salinity and natural inorganic ions

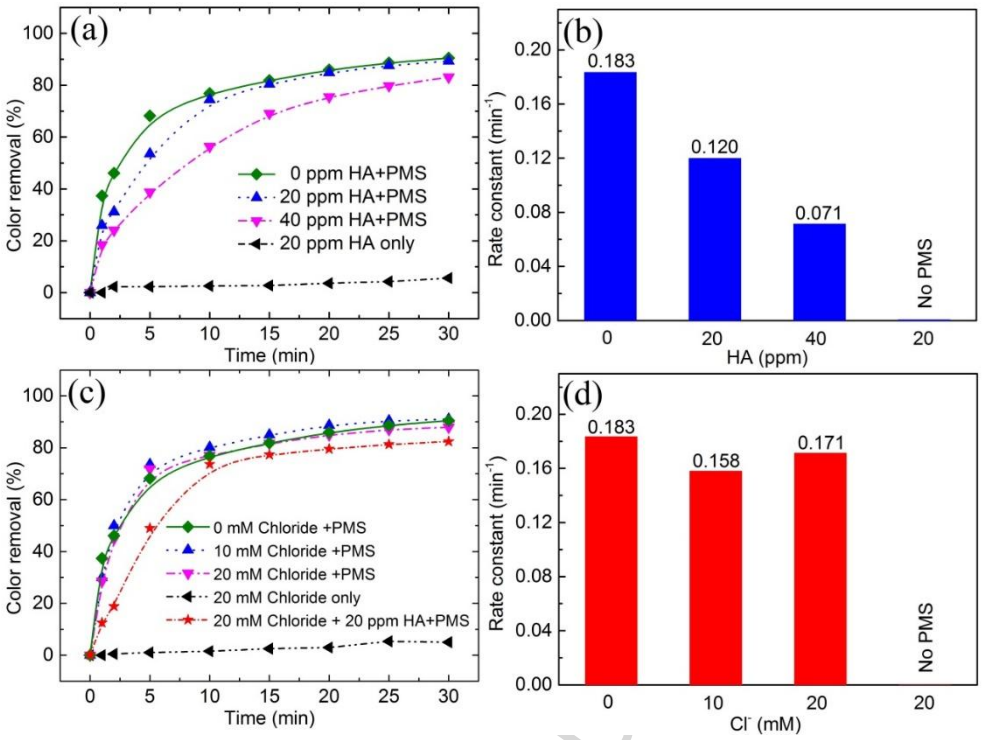

Fig. 6. The effect of (a) humic acid concentration on EY dye color removal, (b) the corresponding reaction kinetics (*k*); (c) chloride ions concentration on EY dye color removal, and (d) the corresponding reaction kinetics (*k*) (catalyst dosage: 0.5 g/L, UV-Vis irradiation intensity: 7.7 μW/cm^2, dye concentration: 100 ppm and PMS concentration: 1.0 mM)

The natural inorganic ions are commonly existing in wastewater that would have impacts on the success of industrial effluents treatment. Humic acids (HA) are produced by biodegradation of dead organic matters and largely exist in aquatic environments. It has been reported that HA have the capability to activate PMS or PS to generate SO_4•$^-$ and •OH [70, 71]. Fig. 6(a) shows the influence of HA initial concentrations on EY dye degradation. Specifically, without the addition of PMS, decolorization rate of EY is only reached about 10% in the presence of HA and $Fe_{73.5}Si_{13.5}B_9Cu_1Nb_3$. Increasing the HA concentration from 0 ppm to 40 ppm could slightly decrease the EY dye degradation efficiency. The experimental results show that the presence of HA in the $Fe_{73.5}Si_{13.5}B_9Cu_1Nb_3$ MGs/PMS system inhibits for EY dye degradation. The likely reasons are: 1) the adsorption of HA molecules to the active sites of the $Fe_{73.5}Si_{13.5}B_9Cu_1Nb_3$ surface are stronger than the dye molecules, resulting

in reducing oxidation efficiency [72]; 2) the inclusion of Cu in the $Fe_{73.5}Si_{13.5}B_9Cu_1Nb_3$ ribbon can increase the formation of inner-sphere complexes with HA, further reducing the effective surface contact area [73]. Fig. 6(b) depicts the pseudo first-order kinetic rate constants k_{obs} with the addition of HA. It can be clearly seen that the reaction rates (k) moderately drop while increase HA initial concentration. The addition of 40 ppm HA in EY dye solution shows the lowest reaction rate of 0.071 min^{-1}. Reducing the HA concentration to 20 ppm, the kinetic rate increases to 0.120 min^{-1}, whereas without adding HA shows the highest kinetic rate of 0.183 min^{-1}. In terms of high concentration of salinity, chloride ion (Cl^-) is one of the major inorganic particles in the natural wastewater. The chloride ion (Cl^-) could scavenge both $SO_4\bullet^-$ (Eq. 12) and •OH (Eq. 13). The redox potential of the generated $Cl_2\bullet^-$ (Eqs. 14 and 15) is 2.1 V, which is much lower than the redox potentials of $SO_4\bullet^-$ (2.5 - 3.1 V) and •OH (2.7 - 2.8 V). Meanwhile, the chloride ion (Cl^-) could also break PMS down to inorganics (Eqs. 16 and 17), resulting in the reduction of the dye degradation efficiency. Fig. 6(c) demonstrates that increasing the Cl^- concentration from 0 mM to 20 mM has no obvious effect on EY degradation efficiency. The reason is that excessive production of $Cl_2\bullet^-$ could quickly compensate the depletion of $SO_4\bullet^-$ and •OH [74]. Fig. 6(d) shows the pseudo first-order kinetic rate constants k with the addition of chloride ions. The results indicate a slight decrease. Therefore, the $Fe_{73.5}Si_{13.5}B_9Cu_1Nb_3$ MGs/PMS system is a very promising treatment method even with a certain amount of Cl^- existing in EY dye water.

$$SO_4\bullet^- + Cl^- \rightarrow SO_4^{2-} + Cl\bullet \quad (12)$$

$$\bullet OH + Cl^- \rightarrow ClOH\bullet^- \quad (13)$$

$$Cl\bullet + Cl^- \rightarrow Cl_2\bullet^- \quad (14)$$

$$ClOH\bullet^- + Cl^- \rightarrow Cl_2\bullet^- + OH^- \quad (15)$$

$$HSO_5^- + Cl^- \rightarrow SO_4^{2-} + HOCl \quad (16)$$

$$HSO_5^- + 2Cl^- + H^+ \rightarrow SO_4^{2-} + Cl_2 + H_2O \quad (17)$$

3.4. Catalytic mechanism

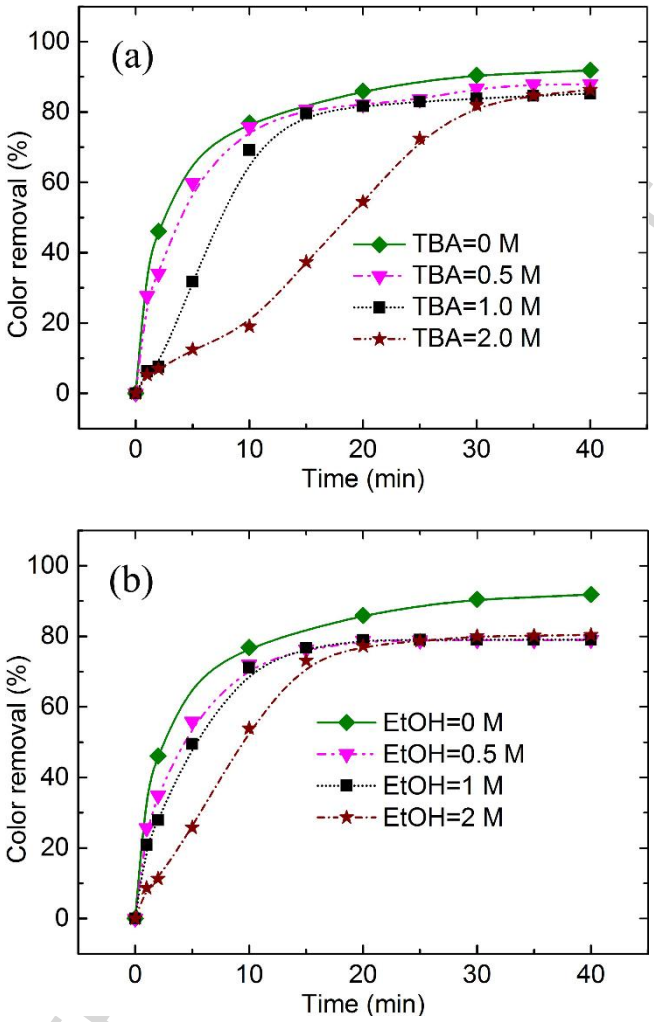

Fig. 7. Effects of quenching agents of (a) TBA and (b) EtOH on EY dye degradation (irradiation intensity: 7.7 μW/cm^2, dye concentration: 100 ppm, catalyst dosage: 0.5g/L, PMS concentration: 1.0 mM)

In order to distinguish the dominant radical species for PMS activation, the tertiary butanol (TBA), and ethanol (EtOH) are chosen as chemical probes for monitoring the generation of •OH [75] and SO_4•$^-$ [76], respectively. Fig. 7(a) shows the effect of the addition of TBA in EY dye degradation. When increasing the TBA concentration from 0 M to 1.0 M, the degradation rate sharply drops from 78% to 30% after 5 min. Further raising the TBA concentration to 2.0 M, the color removal rate decreases to 10% within 5 min. It reveals a significant scavenging effect of •OH by employing TBA. On the other hand, the degradation

rates of EY with three different TBA concentrations (0.5 M, 1.0 M, and 2.0 M) achieve at approximate 78% after 20 min, indicating the produced $SO_4^{\bullet-}$ contributes to the EY degradation. Fig. 7(b) depicts the scavenging influence of EtOH on EY dye degradation. It is observed that the degradation efficiency slightly drops from 76% to 68% within 10 min while increasing EtOH from 0 M to 1.0 M. The degradation rate is slightly reduced in the presence of EtOH, suggesting that the •OH play a dominant role at the first 10 min. Obviously, the color removal rate of EY with three EtOH concentrations (0.5 M, 1.0 M, and 2.0 M) reach at approximate 78% after 20 min, indicating the radical species (•OH) is responsible for the EY dye color removal.

By comparison, such performance denotes that both •OH and $SO_4^{\bullet-}$ are dominant radical species for decolorization of EY dye. It is noted that the EY dye color removal efficiency sharply decreases to 20% within 10 min in the presence of 2.0 M TBA. This result demonstrates that •OH is the dominant radical in the first 10 min and $SO_4^{\bullet-}$ has more impact on the EY dye degradation after 10 min. The mechanism of PMS activation by employing $Fe_{73.5}Si_{13.5}B_9Cu_1Nb_3$ MG is proposed in Fig. 8. The proposed mechanism is that the disordered atomic structure of $Fe_{73.5}Si_{13.5}B_9Cu_1Nb_3$ glassy ribbon has weak atomic bonding, where the electrons around the randomly disordered atoms can be easily activated on the surface of metal. The amorphous Fe^0, acting both electron donator and acceptor, could significantly enhance the electron transfer ability, and the inclusion of Si and B elements would further strengthen the glass-forming ability (GFA) [16] and improve the surface stability [16, 41, 58]. Therefore, the effective electron transfer could enhance the activation efficiency of reactive species [77] from PMS by the $Fe_{73.5}Si_{13.5}B_9Cu_1Nb_3$ glassy ribbons. In addition, the thermostat water bath and UV-vis light are employed in this work could also improve activation efficiency of PMS, thereby increasing the production of •OH and $SO_4^{\bullet-}$ to degrade organic molecules.

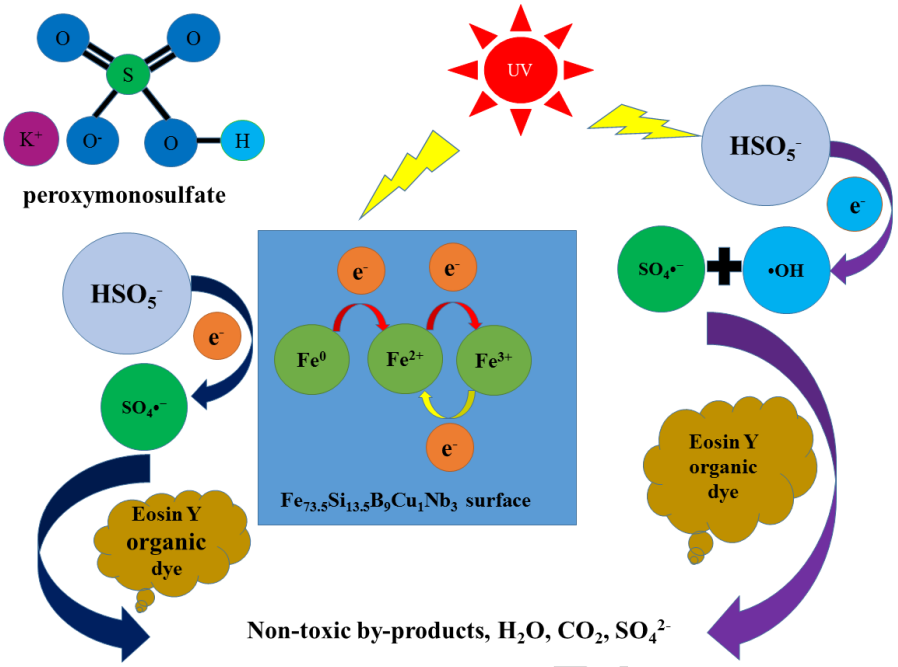

Fig. 8. Schematic illustration of the proposed PMS activation mechanism by using $Fe_{73.5}Si_{13.5}B_9Cu_1Nb_3$ MGs

From previous literatures, the $Fe_{73.5}Si_{13.5}B_9Cu_1Nb_3$ MG has been demonstrated with high potential to activate H_2O_2 [16] and persulfate [41] to rapidly generate •OH and SO_4•$^-$, respectively. The $Fe_{73.5}Si_{13.5}B_9Cu_1Nb_3$ MGs show at least 5 times of reusability for the persulfate activation in malachite green dye degradation [41]. In this work, the $Fe_{73.5}Si_{13.5}B_9Cu_1Nb_3$ MG also shows a high reusability and surface stability in the PMS activation.

3.5. Reusability and surface aging

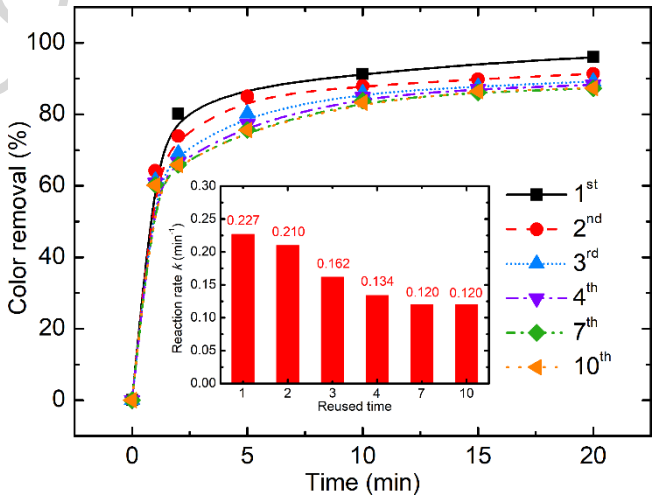

Fig. 9. Color removal rate of Eosin Y dye with reused $Fe_{73.5}Si_{13.5}B_9Cu_1Nb_3$ MGs. inset shows reaction kinetics (*k*) at the corresponding reused time. (Experimental conditions: catalyst dosage: 1.0 g/L, irradiation intensity: 7.7 μW/cm^2, dye concentration: 100 ppm, and PMS concentration: 1.0 mM)

According to Fig. 9, the $Fe_{73.5}Si_{13.5}B_9Cu_1Nb_3$ MGs demonstrate an excellent reusability in the PMS activation for degrading Eosin Y dye even resued 10 times. The dye degradation efficiency slightly decreases after reused for 4 times but all the reactions can achieve 90% of color removal rate in 20 min. The reaction rates for these 4 reused times are 0.227 min^{-1}, 0.210 min^{-1}, 0.162 min^{-1} and 0.134 min^{-1}, respectively. Then the decrease of reaction rate almost terminates after reused 7 times and 10 times, which have a same reaction rate of 0.120 min^{-1}. In order to assess the surface stability of MGs, Fig. 10(a) shows the surface aging of identical MGs after reused 10 times. Although the surface of ribbon has a slight decay with several corrosion areas, most of surface still present relative soomth as as-spun ribbons in the Fig. 1(b). In addition, it can be seen from Fig. 10(b) that there are some precipitations around the corrosion area, which can be comfirmed as Si/Nb oxides. Those precipitation are very similar as reported previously [41], as generated near the rougher areas. According to previous discussion of extreme low Nb leaching concentration in Fig. 4, it can be known that the inclusion of Nb can promote the formation of Nb oxides on the surface, which are very hard for shedding, and enhance the surface stability avoiding fast decay of surface as demonstration in Fig. 10 [16, 41]. Therefore, the activation efficiency of $Fe_{73.5}Si_{13.5}B_9Cu_1Nb_3$ MGs toward PMS in the EY degradation slowly decrease with increasing reused time while the surface decay is very slow.

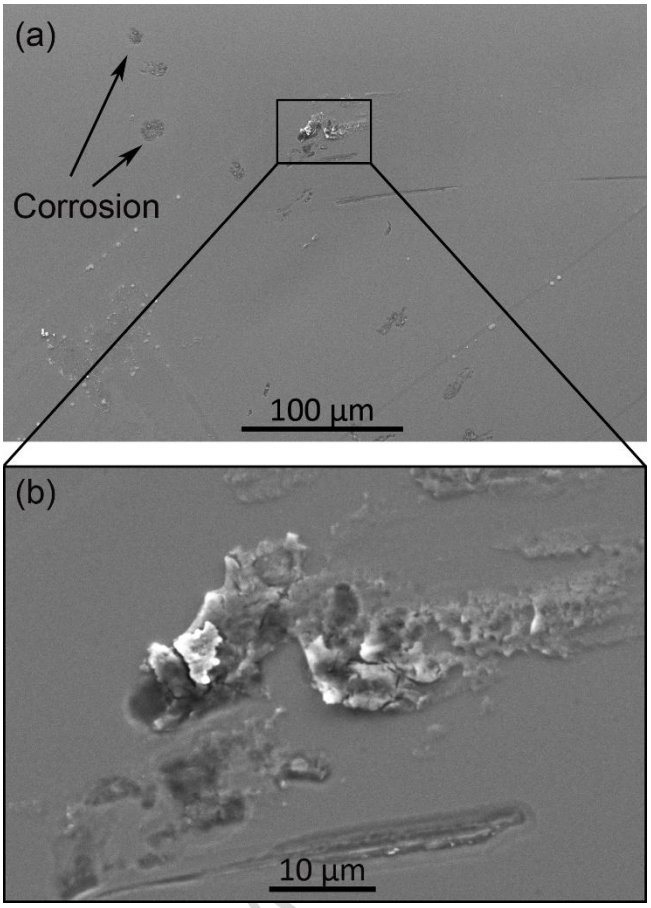

Fig. 10. (a) SEM image of 10 times reused $Fe_{73.5}Si_{13.5}B_9Cu_1Nb_3$ ribbons for activation PMS in the Eosin Y dye degradation and (b) corresponding zoom-in SEM image.

4. Conclusion

This work reports the PMS activation using $Fe_{73.5}Si_{13.5}B_9Cu_1Nb_3$ MGs as catalysts in wastewater treatment. The result shows the low-cost glassy ribbons have excellent performance in catalytic degradation of EY effluents under heterogeneous photo Fenton-like process. The dye degradation processes are well fitted with the pseudo-first-order reaction kinetic model. Compared to the crystalline catalysts, a lower activation energy of E_a = 22.2 kJ/mol is evaluated with Arrhenius equation for $Fe_{73.5}Si_{13.5}B_9Cu_1Nb_3$ MGs that are responsible for the high reactivity of dye treatment. Furthermore, the electrochemical behavior of $Fe_{73.5}Si_{13.5}B_9Cu_1Nb_3$ MGs in simulated dye solution gives the evidence of high

corrosion resistance ability and strong electron transfer ability. The disordered atomic packing structure gives weak atomic bonding in $Fe_{73.5}Si_{13.5}B_9Cu_1Nb_3$ MGs, suggesting fast electron transfer ability during the dye treatment process. The fast generation of $SO_4^{\bullet -}$ and •OH from PMS by $Fe_{73.5}Si_{13.5}B_9Cu_1Nb_3$ MGs are evidenced as the catalytic mechanism for dye degradation. This critical study provides a significant advance in the understanding of electron transfer ability of $Fe_{73.5}Si_{13.5}B_9Cu_1Nb_3$ MGs in the treatment of organic dye effluents and more importantly, gives a great idea to synthesize novel catalysts in dye wastewater treatment.

Acknowledgement

The authors are grateful for the financial supports from the ECU Innovator Awards (Project No. 23641), Australian Research Council Discovery Project (DP130103592) and National Science Foundation of China (Grant No. 51771103).

References

[1] H. Li, S. Pang, Y. Liu, L. Sun, P.K. Liaw, T. Zhang, Biodegradable Mg–Zn–Ca–Sr bulk metallic glasses with enhanced corrosion performance for biomedical applications, Mater. Des. 67 (2015) 9-19.

[2] W.H. Wang, Bulk Metallic Glasses with Functional Physical Properties, Adv. Mater. 21 (2009) 4524-4544.

[3] D.S. Song, J.H. Kim, E. Fleury, W.T. Kim, D.H. Kim, Synthesis of ferromagnetic Fe-based bulk glassy alloys in the Fe–Nb–B–Y system, J. Alloys Compd. 389 (2005) 159-164.

[4] Y. Yang, N. Hua, R. Li, S. Pang, T. Zhang, High-zirconium bulk metallic glasses with high strength and large ductility, Sci. China Phys. Mech. Astron. 56 (2013) 540-544.

[5] A. Baron, D. Szewieczek, G. Nawrat, Corrosion of amorphous and nanocrystalline Fe-based alloys and its influence on their magnetic behavior, Electrochim. Acta 52 (2007) 5690-5695.

[6] J.R. Scully, A. Gebert, J.H. Payer, Corrosion and related mechanical properties of bulk metallic glasses, J. Mater. Res. 22 (2007) 302-313.

[7] P. Ramasamy, M. Stoica, S. Bera, M. Calin, J. Eckert, Effect of replacing Nb with (Mo and Zr) on glass forming ability, magnetic and mechanical properties of FeCoBSiNb bulk metallic glass, J. Alloys Compd. 707 (2017) 78-81.

[8] H.Y. Jung, S.J. Choi, K.G. Prashanth, M. Stoica, S. Scudino, S. Yi, U. Kühn, D.H. Kim, K.B. Kim, J. Eckert, Fabrication of Fe-based bulk metallic glass by selective laser melting: a parameter study, Mater. Des. 86 (2015) 703-708.

[9] A.L. Greer, Y.Q. Cheng, E. Ma, Shear bands in metallic glasses, Mater. Sci. Eng. R Rep. 74 (2013) 71-132.

[10] M. Ghidelli, S. Gravier, J.J. Blandin, P. Djemia, F. Mompiou, G. Abadias, J.P. Raskin, T. Pardoen, Extrinsic mechanical size effects in thin ZrNi metallic glass films, Acta Mater. 90 (2015) 232-241.

[11] M. Ghidelli, H. Idrissi, S. Gravier, J.J. Blandin, J.P. Raskin, D. Schryvers, T. Pardoen, Homogeneous flow and size dependent mechanical behavior in highly ductile $Zr_{65}Ni_{35}$ metallic glass films, Acta Mater. 131 (2017) 246-259.

[12] J.Q. Wang, Y.H. Liu, M.W. Chen, D.V. Louzguine Luzgin, A. Inoue, J.H. Perepezko, Excellent capability in degrading azo dyes by MgZn-based metallic glass powders, Sci. Rep. 2 (2012) 418.

[13] P. Wang, X. Bian, Y. Li, Catalytic oxidation of phenol in wastewater - a new application of the amorphous $Fe_{78}Si_9B_{13}$ alloy, Chin. Sci. Bull. 57 (2012) 33-40.

[14] P. Wang, J.Q. Wang, H. Li, H. Yang, J. Huo, J. Wang, C. Chang, X. Wang, R. Li, G. Wang, Fast decolorization of azo dyes in both alkaline and acidic solutions by Al-based metallic glasses, J. Alloys Compd. 701 (2017) 759-767.

[15] P. Liu, J.L. Zhang, M.Q. Zha, C.H. Shek, Synthesis of an Fe rich amorphous structure with a catalytic effect to rapidly decolorize azo dye at room temperature, ACS Appl. Mater. Interfaces 6 (2014) 5500-5505.

[16] Z. Jia, J. Kang, W.C. Zhang, W.M. Wang, C. Yang, H. Sun, D. Habibi, L.C. Zhang, Surface aging behaviour of Fe-based amorphous alloys as catalysts during heterogeneous photo Fenton-like process for water treatment, Appl. Catal. B Environ. 204 (2017) 537-547.

[17] S. Xie, P. Huang, J.J. Kruzic, X. Zeng, H. Qian, A highly efficient degradation mechanism of methyl orange using Fe-based metallic glass powders, Sci. Rep. 6 (2016) 21947.

[18] Z. Jia, X. Duan, W.C. Zhang, W.M. Wang, H. Sun, S. Wang, C. Yang, L.C. Zhang, Ultra-sustainable $Fe_{78}Si_9B_{13}$ metallic glass as a catalyst for activation of persulfate on methylene blue degradation under UV-Vis light, Sci. Rep. 6 (2016) 38520.

[19] M. Kositzi, A. Antoniadis, I. Poulios, I. Kiridis, S. Malato, Solar photocatalytic treatment of simulated dyestuff effluents, Sol. Energy 77 (2004) 591-600.

[20] T. Torres-Blancas, G. Roa-Morales, F. Ureña-Núñez, C. Barrera-Díaz, A. Dorazco-González, R. Natividad, Ozonation enhancement by Fe–Cu biometallic particles, J. Taiwan Inst. Chem. Eng. 74 (2017) 225-232.

[21] Z. Jia, W.C. Zhang, W.M. Wang, D. Habibi, L.C. Zhang, Amorphous $Fe_{78}Si_9B_{13}$ alloy: an efficient and reusable photo-enhanced Fenton-like catalyst in degradation of cibacron brilliant red 3B-A dye under UV–vis light, Appl. Catal. B Environ. 192 (2016) 46-56.

[22] S.X. Liang, Z. Jia, W.C. Zhang, X.F. Li, W.M. Wang, H.C. Lin, L.C. Zhang, Ultrafast activation efficiency of three peroxides by $Fe_{78}Si_9B_{13}$ metallic glass under photo-enhanced catalytic oxidation: a comparative study, Appl. Catal. B Environ. 221 (2018) 108-118.

[23] S. Xavier, R. Gandhimathi, P.V. Nidheesh, S.T. Ramesh, Comparison of homogeneous and heterogeneous Fenton processes for the removal of reactive dye magenta MB from aqueous solution, Desalin. Water Treat. 53 (2015) 109-118.

[24] J. Miao, Z. Jia, H.B. Lu, D. Habibi, L.C. Zhang, Heterogeneous photocatalytic degradation of mordant black 11 with ZnO nanoparticles under UV–Vis light, J. Taiwan Inst. Chem. Eng. 45 (2014) 1636-1641.

[25] Z. Jia, J. Miao, H.B. Lu, D. Habibi, W.C. Zhang, L.C. Zhang, Photocatalytic degradation and absorption kinetics of cibacron brilliant yellow 3G-P by nanosized ZnO catalyst under simulated solar light, J. Taiwan Inst. Chem. Eng. 60 (2016) 267-274.

[26] J.J. Murcia, M.C. Hidalgo, J.A. Navío, J. Araña, J.M. Doña-Rodríguez, Study of the phenol photocatalytic degradation over TiO_2 modified by sulfation, fluorination, and platinum nanoparticles photodeposition, Appl. Catal. B Environ. 179 (2015) 305-312.

[27] G.B. Ortiz de la Plata, O.M. Alfano, A.E. Cassano, Optical properties of goethite catalyst for heterogeneous photo-Fenton reactions: comparison with a titanium dioxide catalyst, Chem. Eng. J. 137 (2008) 396-410.

[28] M. Usman, P. Faure, K. Hanna, M. Abdelmoula, C. Ruby, Application of magnetite catalyzed chemical oxidation (Fenton-like and persulfate) for the remediation of oil hydrocarbon contamination, Fuel 96 (2012) 270-276.

[29] Q. Lan, F.B. Li, C.X. Sun, C.S. Liu, X.Z. Li, Heterogeneous photodegradation of pentachlorophenol and iron cycling with goethite, hematite and oxalate under UVA illumination, J. Hazard. Mater. 174 (2010) 64-70.

[30] L.C.A. Oliveira, M. Gonçalves, M.C. Guerreiro, T.C. Ramalho, J.D. Fabris, M.C. Pereira, K. Sapag, A new catalyst material based on niobia/iron oxide composite on the oxidation of organic contaminants in water via heterogeneous Fenton mechanisms, Appl. Catal. A Gen. 316 (2007) 117-124.

[31] I. Grčić, S. Papić, K. Žižek, N. Koprivanac, Zero-valent iron (ZVI) Fenton oxidation of reactive dye wastewater under UV-C and solar irradiation, Chem. Eng. J. 195–196 (2012) 77-90.

[32] J.Q. Wang, Y.H. Liu, M.W. Chen, G.Q. Xie, D.V. Louzguine Luzgin, A. Inoue, J.H. Perepezko, Rapid degradation of azo dye by Fe-based metallic glass powder, Adv. Funct. Mater. 22 (2012) 2567-2570.

[33] Z. Jia, S.X. Liang, W.C. Zhang, W.M. Wang, C. Yang, L.C. Zhang, Heterogeneous photo Fenton-like degradation of cibacron brilliant red 3B-A dye using amorphous $Fe_{78}Si_9B_{13}$ and $Fe_{73.5}Si_{13.5}B_9Cu_1Nb_3$ alloys: the influence of adsorption, J. Taiwan Inst. Chem. Eng. 71 (2017) 128-136.

[34] P. Wardman, Reduction potentials of one-electron couples involving free radicals in aqueous solution, J. Phys. Chem. Ref. Data 18 (1989) 1637-1755.

[35] Y. Xu, Z. Lin, Y. Wang, H. Zhang, The UV/peroxymonosulfate process for the mineralization of artificial sweetener sucralose, Chem. Eng. J. 317 (2017) 561-569.

[36] P. Neta, R.E. Huie, A.B. Ross, Rate constants for reactions of inorganic radicals in aqueous solution, J. Phys. Chem. Ref. Data 17 (1988) 1027-1284.

[37] M.L. Crimi, J. Taylor, Experimental evaluation of catalyzed hydrogen peroxide and sodium persulfate for destruction of BTEX contaminants, Soil Sediment Contam. 16 (2007) 29-45.

[38] P.V. Nidheesh, R. Rajan, Removal of rhodamine B from a water medium using hydroxyl and sulphate radicals generated by iron loaded activated carbon, RSC Adv. 6 (2016) 5330-5340.

[39] Y. Ren, L. Lin, J. Ma, J. Yang, J. Feng, Z. Fan, Sulfate radicals induced from peroxymonosulfate by magnetic ferrospinel MFe_2O_4 (M = Co, Cu, Mn, and Zn) as heterogeneous catalysts in the water, Appl. Catal. B Environ. 165 (2015) 572-578.

[40] Z. Jia, J.C. Wang, S.X. Liang, W.C. Zhang, W.M. Wang, L.C. Zhang, Activation of peroxymonosulfate by $Fe_{78}Si_9B_{13}$ metallic glass: the influence of crystallization, J. Alloys Compd. 728 (2017) 525-533.

[41] S.X. Liang, Z. Jia, W.C. Zhang, W.M. Wang, L.C. Zhang, Rapid malachite green degradation using $Fe_{73.5}Si_{13.5}B_9Cu_1Nb_3$ metallic glass for activation of persulfate under UV–Vis light, Mater. Des. 119 (2017) 244-253.

[42] P. Xie, J. Ma, W. Liu, J. Zou, S. Yue, X. Li, M.R. Wiesner, J. Fang, Removal of 2-MIB and geosmin using UV/persulfate: contributions of hydroxyl and sulfate radicals, Water Res. 69 (2015) 223-33.

[43] Y. Ji, C. Dong, D. Kong, J. Lu, Q. Zhou, Heat-activated persulfate oxidation of atrazine: implications for remediation of groundwater contaminated by herbicides, Chem. Eng. J. 263 (2015) 45-54.

[44] H. Chen, K.C. Carroll, Metal-free catalysis of persulfate activation and organic-pollutant degradation by nitrogen-doped graphene and aminated graphene, Environ. Pollut. 215 (2016) 96-102.

[45] L. Zhao, H. Hou, A. Fujii, M. Hosomi, F. Li, Degradation of 1,4-dioxane in water with heat- and Fe(2+)-activated persulfate oxidation, Environ. Sci. Pollut. Res. Int. 21 (2014) 7457-65.

[46] C. Liang, Y.Y. Guo, Mass transfer and chemical oxidation of naphthalene particles with zerovalent iron activated persulfate, Environ. Sci. Technol. 44 (2010) 8203-8208.

[47] A. Alvarez-Martin, S. Trashin, M. Cuykx, A. Covaci, K. De Wael, K. Janssens, Photodegradation mechanisms and kinetics of Eosin-Y in oxic and anoxic conditions, Dyes Pigm. 145 (2017) 376-384.

[48] A. Bafana, S.S. Devi, T. Chakrabarti, Azo dyes: past, present and the future, Environ. Rev. 19 (2011) 350-371.

[49] L.C. Zhang, J. Xu, Glass-forming ability of melt-spun multicomponent (Ti, Zr, Hf)–(Cu, Ni, Co)–Al alloys with equiatomic substitution, J. Non-Cryst. Solids 347 (2004) 166-172.

[50] L.C. Zhang, Z.Q. Shen, J. Xu, Mechanically milling-induced amorphization in Sn-containing Ti-based multicomponent alloy systems, Mater. Sci. Eng. A 394 (2005) 204-209.

[51] L.C. Zhang, K.B. Kim, P. Yu, W.Y. Zhang, U. Kunz, J. Eckert, Amorphization in mechanically alloyed (Ti, Zr, Nb)–(Cu, Ni)–Al equiatomic alloys, J. Alloys Compd. 428 (2007) 157-163.

[52] S.D. Zhang, W.L. Zhang, S.G. Wang, X.J. Gu, J.Q. Wang, Characterisation of three-dimensional porosity in an Fe-based amorphous coating and its correlation with corrosion behaviour, Corros. Sci. 93 (2015) 211-221.

[53] H.B. Lu, L.C. Zhang, A. Gebert, L. Schultz, Pitting corrosion of Cu–Zr metallic glasses in hydrochloric acid solutions, J. Alloys Compd. 462 (2008) 60-67.

[54] L. Chen, Q. Zeng, J. Li, J. Lu, Y. Zhang, L. Zhang, X. Qin, W. Lu, L. Zhang, L. Wang, D. Zhang, Effect of microstructure on corrosion behavior of a Zr–Sn–Nb–Fe–Cu–O alloy, Mater. Des. 92 (2016) 888-896.

[55] Z. Jia, X. Duan, P. Qin, W.C. Zhang, W.M. Wang, C. Yang, H. Sun, S. Wang, L.C. Zhang, Disordered atomic packing structure of metallic glass: toward ultrafast hydroxyl radicals production rate and strong electron transfer ability in catalytic performance, Adv. Funct. Mater. 27 (2017) 1702258.

[56] S. Geng, J. Sun, L. Guo, Effect of sandblasting and subsequent acid pickling and passivation on the microstructure and corrosion behavior of 316L stainless steel, Mater. Des. 88 (2015) 1-7.

[57] S. Ehtemam-Haghighi, Y. Liu, G. Cao, L.C. Zhang, Phase transition, microstructural evolution and mechanical properties of Ti-Nb-Fe alloys induced by Fe addition, Mater. Des. 97 (2016) 279-286.

[58] Y. Tang, Y. Shao, N. Chen, K.F. Yao, Rapid decomposition of Direct Blue 6 in neutral solution by Fe–B amorphous alloys, RSC Adv. 5 (2015) 6215-6221.

[59] H. Fang, N. Li, Z. Xue, Y. Zhang, Y. Zheng, X. Tao, Efficient charge separation promoting visible-light-driven photocatalytic activity of MnO_x decorated WS2 hybrid nanosheets, Electrochem. Commun. 72 (2016) 118-121.

[60] N. Dai, L. Zhang, J. Zhang, X. Zhang, Q. Ni, Y. Chen, M. Wu, C. Yang, Distinction in corrosion resistance of selective laser melted Ti-6Al-4V alloy on different planes, Corros. Sci. 111 (2016) 703-710.

[61] F. Ghanbari, M. Moradi, Application of peroxymonosulfate and its activation methods for degradation of environmental organic pollutants: review, Chem. Eng. J. 310 (2017) 41-62.

[62] K. Vignesh, A. Suganthi, M. Rajarajan, R. Sakthivadivel, Visible light assisted photodecolorization of eosin-Y in aqueous solution using hesperidin modified TiO_2 nanoparticles, Appl. Surf. Sci. 258 (2012) 4592-4600.

[63] K. Sarath, R. Gandhimathi, S.T. Ramesh, P.V. Nidheesh, Removal of reactive magenta-MB from aqueous solution by persulphate-based advanced oxidation process, Desalin. Water Treat. 57 (2016) 11872-11878.

[64] H. Zheng, Y. Pan, X. Xiang, Oxidation of acidic dye eosin Y by the solar photo-Fenton processes, J. Hazard. Mater. 141 (2007) 457-464.

[65] M. Rashid, N.T. Price, M.Á. Gracia Pinilla, K.E. O'Shea, Effective removal of phosphate from aqueous solution using humic acid coated magnetite nanoparticles, Water Res. 123 (2017) 353-360.

[66] Z. Deng, X.H. Zhang, K.C. Chan, L. Liu, T. Li, Fe-based metallic glass catalyst with nanoporous surface for azo dye degradation, Chemosphere 174 (2017) 76-81.

[67] J. Fan, Y. Guo, J. Wang, M. Fan, Rapid decolorization of azo dye methyl orange in aqueous solution by nanoscale zerovalent iron particles, J. Hazard. Mater. 166 (2009) 904-910.

[68] X. Liu, Z. Chen, Z. Chen, M. Megharaj, R. Naidu, Remediation of direct black G in wastewater using kaolin-supported bimetallic Fe/Ni nanoparticles, Chem. Eng. J. 223 (2013) 764-771.

[69] J. Chen, L. Zhu, Heterogeneous UV-Fenton catalytic degradation of dyestuff in water with hydroxyl-Fe pillared bentonite, Catal. Today 126 (2007) 463-470.

[70] M. Ahmad, A.L. Teel, R.J. Watts, Mechanism of persulfate activation by phenols, Environ. Sci. Technol. 47 (2013) 5864-5871.

[71] G. Fang, J. Gao, D.D. Dionysiou, C. Liu, D. Zhou, Activation of persulfate by quinones: free radical reactions and implication for the degradation of PCBs, Environ. Sci. Technol. 47 (2013) 4605-4611.

[72] F. Wang, Y. Wu, Y. Gao, H. Li, Z. Chen, Effect of humic acid, oxalate and phosphate on Fenton-like oxidation of microcystin-LR by nanoscale zero-valent iron, Sep. Purif. Technol. 170 (2016) 337-343.

[73] Y. Qi, J. Zhu, Q. Fu, H. Hu, Q. Huang, Sorption of Cu by humic acid from the decomposition of rice straw in the absence and presence of clay minerals, J. Environ. Manage. 200 (2017) 304-311.

[74] X. Sun, Y. Ding, B. Zhang, R. Huang, D. Chen, D.S. Su, Insight into the enhanced selectivity of phosphate-modified annealed nanodiamond for oxidative dehydrogenation reactions, ACS Catal. 5 (2015) 2436-2444.

[75] I. Stranic, G.A. Pang, R.K. Hanson, D.M. Golden, C.T. Bowman, Shock tube measurements of the tert-butanol + OH reaction rate and the tert-C_4H_8OH radical beta-scission branching ratio using isotopic labeling, J. Phys. Chem. A 117 (2013) 4777-4784.

[76] Y. Wang, H. Sun, X. Duan, H.M. Ang, M.O. Tadé, S. Wang, A new magnetic nano zero-valent iron encapsulated in carbon spheres for oxidative degradation of phenol, Appl. Catal. B Environ. 172-173 (2015) 73-81.

[77] Y. Bu, Z. Chen, W. Li, Using electrochemical methods to study the promotion mechanism of the photoelectric conversion performance of Ag-modified mesoporous g-C_3N_4 heterojunction material, Appl. Catal. B Environ. 144 (2014) 622-630.

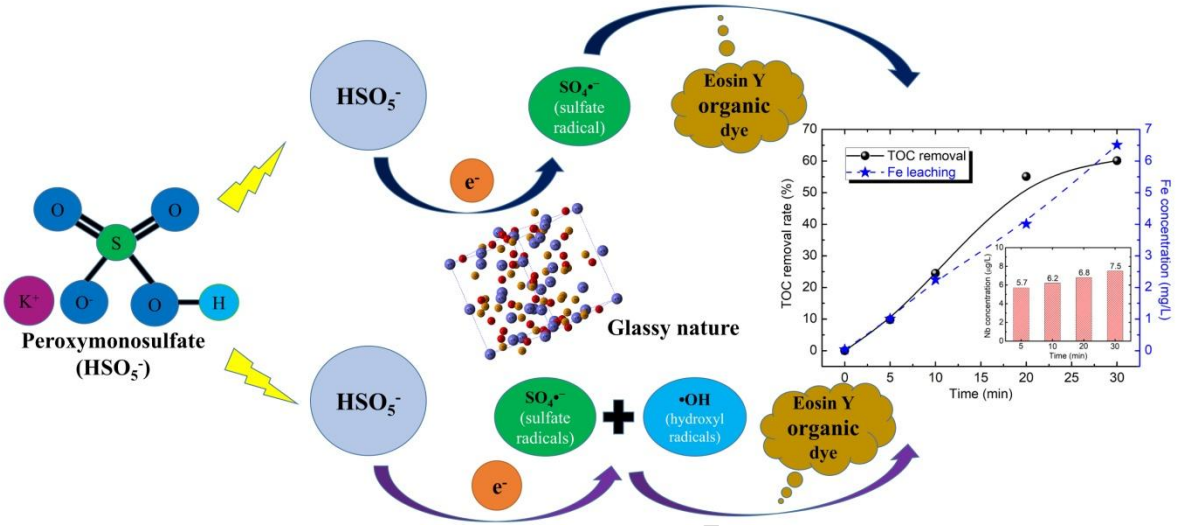

Graphical abstract

Highlights

- Strong electron transfer ability of $Fe_{73.5}Si_{13.5}B_9Cu_1Nb_3$ metallic glasses has been studied.
- The peroxymonosulfate activation as a function of various parameters has been investigated.
- 100% of Eosin Y degradation has been achieved within 20 min under rational experiment control.
- The catalytic mechanism of photo-enhanced peroxymonosulfate activation by $Fe_{73.5}Si_{13.5}B_9Cu_1Nb_3$ metallic glasses has been discussed.